Chinese Chemical Letters 37 (2026) 111436

Contents lists available at ScienceDirect

Chinese Chemical Letters

journal homepage: www.elsevier.com/locate/cclet

Defect engineering using Ti-doped calcium niobate nanosheets in polymer-based dielectrics for high temperature capacitance

Dongyang Chen[a], Xiaoxu Liu[a,*], Haonan Chen[a], Yaru Wang[a], Jing Li[a], Jiaming Sun[a], Xiaofeng Wang[b,*], Qiong Liu[c]

[a] School of Materials Science and Engineering, Shaanxi Key Laboratory of Green Preparation and Functionalization for Inorganic Materials, Shaanxi University of Science and Technology, Xi'an 710021, China
[b] School of Mechanical and Electrical Engineering, Shaanxi University of Science and Technology, Xi'an 710021, China
[c] Xi 'an Herong New Energy Technology Co., Ltd., Xi'an 710021, China

ARTICLE INFO

Article history:
Received 27 April 2025
Revised 9 June 2025
Accepted 10 June 2025
Available online 10 June 2025

Keywords:
Defect engineering
Titanium-doped calcium niobate nanosheets
Inorganic-organic interface
Polymer dielectrics
High temperature capacitance

ABSTRACT

Although the incorporation of fillers has improved the high temperature (150–200 °C) capacitance of polymer composite dielectrics, effective strategies for designing filler-matrix interface structures remains a formidable challenge. Herein, defect-rich nanosheets ($Ca_2Nb_{2.75}Ti_{0.25}O_{10}$, CT) were coated with a zeolite imidazolate frameworks-8 (ZIF-8, $Zn(C_4H_5N_2)_2$) layer (mCT). The mCT was integrated into polyetherimide (PEI) to create the polymer-based dielectrics. The defects on the surface of the negative CT nanosheets exhibited strong anchoring effects on the Zn^{2+} in ZIF-8, enhancing the filler-coating layer interface. Additionally, X-ray absorption fine structure analysis and density functional theory confirmed that the porous ZIF-8 coating layer forms strong coordination bonds with the PEI molecular chains, thereby an increased band gap (3.3 eV) of PEI/mCT compared to PEI (3.0 eV). It demonstrated exceptional performance at high temperatures, achieving ultra-high energy storage densities of 5.25 and 4.47 J/cm^3 with efficiency >90% at 150 and 200 °C, which are higher than PEI (0.4 and 0.4 J/cm^3). This work offers a new approach and reference for designing high-temperature polymer composite dielectrics for energy storage applications.

© 2026 Published by Elsevier B.V. on behalf of Chinese Chemical Society and Institute of Materia Medica, Chinese Academy of Medical Sciences.

Polymer capacitors are known for their high-power density, voltage resistance, and exceptional reliability, advancing modern power electronic systems [1–7]. There is a growing demand for polymer capacitors capable of operating at extreme temperatures (150–200 °C) in applications such as hybrid electric vehicles, oil and gas exploration, and wind generators [8–12]. However, commercially available biaxially oriented polypropylene (BOPP) struggles at high temperatures [13], leading to the development of high glass transition temperature polymers like Kapton (PI), ULTEM (PEI) and ISARYL (FPE) for high-temperature dielectric capacitors [14]. These polymers often exhibit exponentially increasing conduction currents with temperature and electric field, reducing discharge energy density (U_e) and limiting their industrial application as dielectrics [15,16]. Research has led to strategies to suppress high-temperature conductivity and enhance energy storage properties of polymer-based dielectrics [17,18]. For example, cross-linked c-BCB with BNNs nanosheets shows a tenfold reduction in conductivity and impressive energy storage (1.6 J/cm^3 at 200 °C, η > 90%) [19]. Physical cross-linking in PI-based polymers achieves 4.0 J/cm^3 with η > 90% at 200 °C [20]. Additionally, wide bandgap nanofillers like Si_3N_4, BNNs, Al_2O_3, and SiO_2 [21–24] have been used to create barriers at the electrode-polymer dielectric interface, improving capacitive performance by suppressing charge injection. Inorganic nanofillers with high thermal stability, such as BNNs, HfO_2, Al_2O_3 [25], and SiO_2 [26], alter the energy levels of polymer dielectrics, improving performance by inducing charge traps and capturing hot carriers [27–30]. Most methods focus on the filler-polymer structure, but the inorganic-organic interface significantly impacts insulation and capacitive performance [17,18,31]. Our previous research has shown that hierarchical nanofillers (CNO@Al_2O_3) [32] and organic-metal hybrid interfaces (MOHI) enhance polymer capacitor energy storage performance [33]. Interface structure design is thus a promising strategy for developing advanced polymer dielectrics.

In this work, we present a novel strategy for enhancing high-temperature energy storage in polymer dielectrics by incorporating defect-engineered $Ca_2Nb_{2.75}Ti_{0.25}O_{10}$ (CT) nanosheets. The defect sites facilitate the tight growth of ZIF-8, which introduces low-

* Corresponding authors.
E-mail addresses: xiaoxuliu@sust.edu.cn (X. Liu), ansteelmaker@163.com (X. Wang).

https://doi.org/10.1016/j.cclet.2025.111436
1001-8417/© 2026 Published by Elsevier B.V. on behalf of Chinese Chemical Society and Institute of Materia Medica, Chinese Academy of Medical Sciences.

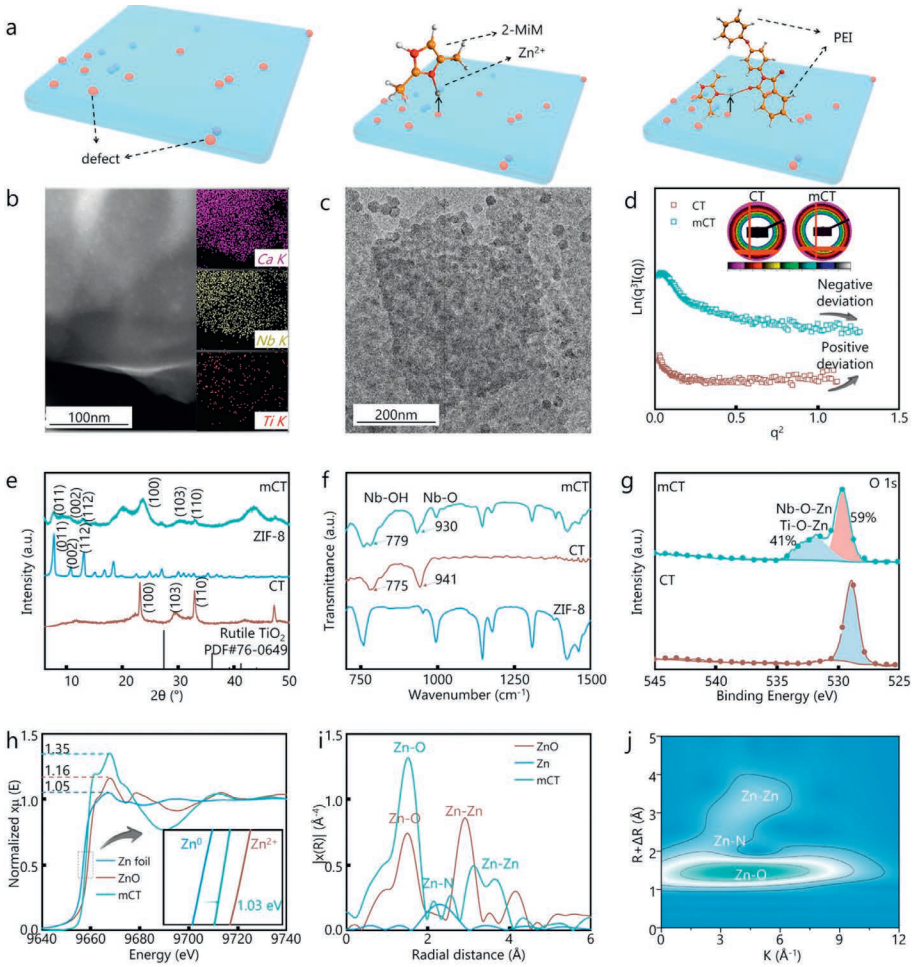


Fig. 1. Morphological and structural characterization of CT, ZIF-8 and mCT: (a) Schematic diagram of interface layer growth induced by defect engineering. (b) Dark field image and elemental mapping. (c) TEM image. (d) The Porod curves. (e) XRD pattern. (f) FT-IR spectrum. (g) XPS O 1s core-level spectrum. (h) Normalized K-edge XANES absorption spectra of Zn element. (i) K-edge FT-EXAFS in R space. (j) Wavelet transformation analysis.

coordinated Zn^{2+} capable of forming coordination bonds with the polymer. This interaction effectively suppresses carbonyl relaxation. As a result, the composite dielectric achieves a remarkable discharged energy density of 4.47 J/cm^3 at 200 °C with an efficiency exceeding 90 %, even at a low filler loading 0.5 wt%. This work provides a new strategy for designing polymer dielectrics with outstanding high temperature capacitance.

The mechanism diagram of the coordination between metal ions and organic compounds induced by Ti-doped calcium niobate ($Ca_2Nb_{2.75}Ti_{0.25}O_{10}$, CT) nanosheets is shown in Fig. 1a. The CT nanosheets were prepared *via* solid-phase reaction. As shown in Fig. S1a (Supporting information), the X-ray diffraction (XRD) pattern of pre-CT exhibits weak (001), (002) and (003) diffraction peaks compared to Ti-undoped nanosheets reported previously [33], indicating altered interlayer spacing and reduced ordering (Fig. S1b in Supporting information). The transmission electron microscopy (TEM) in Fig. S2 (Supporting information) reveales the typical 2D stacked morphology of CT, while element mapping (Fig. 1b) confirms Ti incorporation. Subsequently, ZIF-8 (zeolitic imidazolate framework-8) was coated onto CT to produce the modified nanosheets (mCT).

TEM image of mCT (Fig. 1c) shows the granular morphology of ZIF-8, confirming the successful coating of ZIF-8 on the CT. The electron density fluctuations in nanosheets were examined using small angle X-ray scattering (SAXS). As shown in Fig. 1d, the positive deviation at the CT Porod curve tail indicates that CT exhibits electron density fluctuations or non-uniform regions attributed to defects caused by Ti doping [34]. The negative deviation at the mCT Porod curve tail suggests the presence of dispersed transition layer. This transition layer arises from the physical and chemical interactions between CT and ZIF-8. In Fig. 1e, the XRD pattern of mCT exhibits a notable decrease intensity of ZIF-8. The Fourier transform infrared spectroscopy (FT-IR) results show the presence of ZIF-8 in mCT (Fig. 1f). Additionally, the Nb-OH absorption peak exhibits bule shift from 775 cm^{-1} to 779 cm^{-1}, and the Nb-O absorption peak shows red shift from 941 cm^{-1} to 930 cm^{-1} [32]. These shifts are attributed to the consumption of -OH groups during the interactions of Nb-O-Zn or Ti-O-Zn between ZIF-8 and CT. The X-ray photoelectron spectroscopy (XPS) analysis of nanosheets is shown in Fig. 1f, Figs. S3 and S4 (Supporting information). The additional peak of mCT (Fig. 1g) appeared at 532.0 eV can be ascribed to the interactions between ZIF-8 and CT, which hinders the electron transition of O elements in mCT. The strong interactions are also evidenced in the substantial peak area proportion (28.9 %). The X-ray absorption fine structure (XAFS) measurements provided coordination information of Zn^{2+} in the mCT. As shown in Fig. 1h, the K-Edge of mCT displays a higher white line (WL) peak energy intensity (1.35) compared to Zn foil (1.05) and ZnO (1.16), and the K-Edge of mCT lies between Zn foil and ZnO. These results indicate that Zn in ZIF-8 possesses unoccupied orbitals, which serve as available sites for coordination bonding with PEI [35]. Extended X-ray absorption fine structure (EXAFS) analysis of mCT

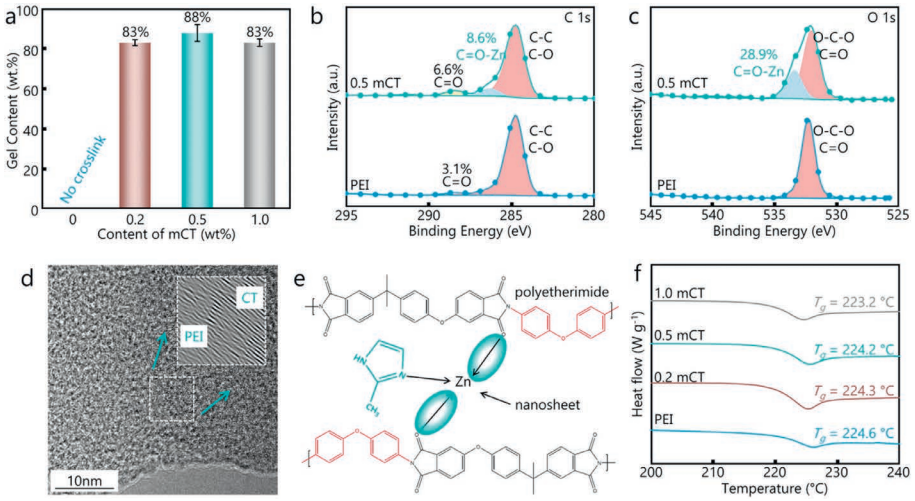


Fig. 2. (a) Gel content in x mCT. XPS of x mCT. (b) C 1s and (c) O 1s core-level spectrum. (d) TEM image and FFT image of 0.5 mCT. (e) Schematic diagram of the interactions between PEI and mCT. (f) DSC curves of x mCT.

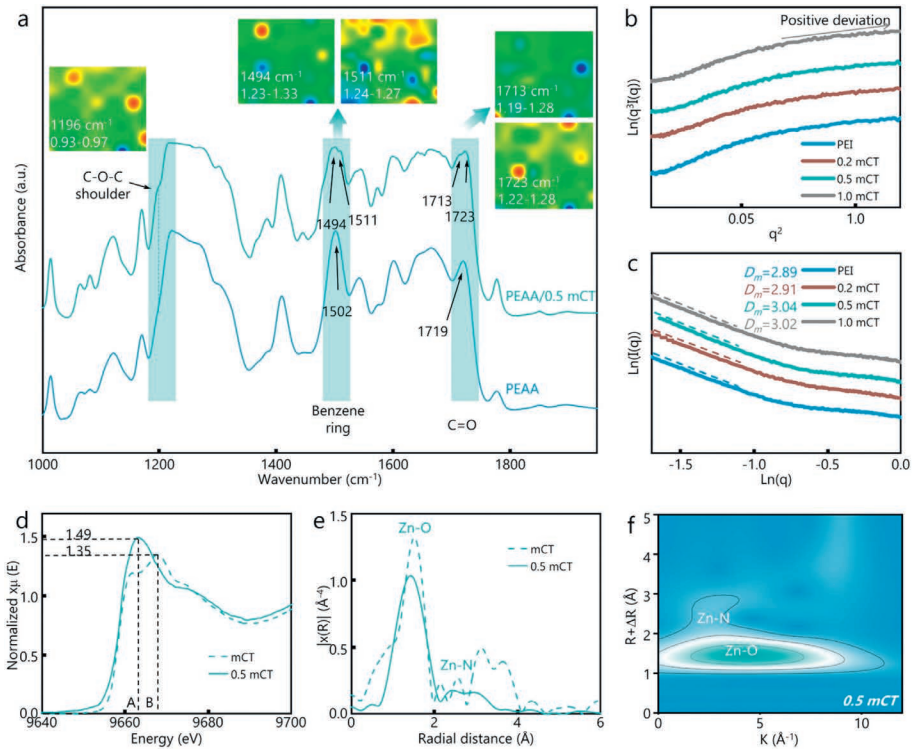


Fig. 3. (a) Spectral comparison of PEAA and PEAA/0.5 mCT and spatially resolved infrared mapping of PEAA/0.5 mCT. The data is the average value of different region, PEAA is polyether amide acid. (b) Porod curves and (c) ln(q)-ln($I(q)$) plots derived from SAXS (Small Angle X-ray Scattering) of x mCT. (d) Normalized K-edge XANES absorption spectra of Zn element. (e) K-edge FT-EXAFS in R space. (f) Wavelet transformation analysis of 0.5 mCT.

(Fig. 1i) confirmed the coordination environments involving Zn-N, Zn-O and Zn-Zn coordination. Detailed coordination parameters are provided in Table S1 (Supporting information). The Wavelet Transform (WT) plot of mCT in Fig. 1j provides evidence of Zn-N, Zn-O and Zn-Zn coordination in K-space.

Polymer dielectrics containing mCT were synthesized *via in situ* polymerization and designated as x mCT (PEI/x wt% mCT, $x = 0$, 0.2, 0.5 and 1.0). As shown in Fig. S5 (Supporting information) and Fig. 2a, PEI shows no gel after soaking in NMP 24 h, whereas 0.5 mCT exhibits optimal gel content (88 %). Scanning electron microscopy of the x mCT (Fig. S6 in Supporting information) demonstrated that those with low filler loading are dense. Polymer dielectrics containing mCT also exhibit low surface energy. Figs. S7 and S8 (Supporting information) exhibit the increased water contact angle and a low root-mean-square value of 0.5 mCT, which are advantageous for the metallization of polymer dielectrics [36]. The chemical interaction between mCT and PEI is further supported by the C=O-Zn coordination peak (Figs. 2b and c). Two factors facilitate the formation of C=O-Zn coordination bonds: First, the presence of Zn^{2+} with unoccupied orbitals in mCT, as confirmed in Fig. 1h; Second, the oxygen atoms in the C=O groups of PEI possess lone pair electrons. To directly investigate the interaction between ZIF-8 and PEI, TEM was employed to observe the microregions of 0.5 mCT. As shown in Fig. 2d, no ZIF-8 particles were observed, and no nanoscale defects or free volume were detected at the CT-PEI interface region, which is consistent with the SEM

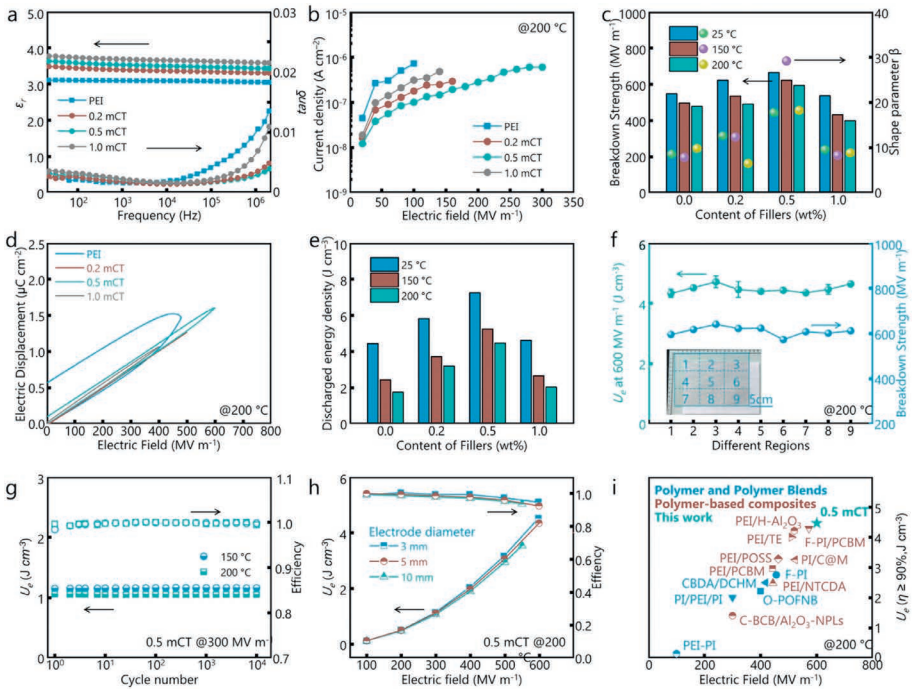


Fig. 4. (a) Frequency dependence of dielectric constant (ε_r) and tanδ at 25 °C of x mCT. (b) The current density of x mCT at 200 °C. (c) Weibull distribution of measured E_b for x mCT at 25, 150 and 200 °C. (d) *D-E* loops of x mCT. (e) Discharge energy density of x mCT. (f) Energy storage performance of different regions in large-scale 0.5 mCT. The insets are the photographs of 0.5 mCT. (g) Cyclic performance of 0.5 mCT at 150 and 200 °C under 300 MV/m. (h) Energy storage performance with different electrode diameter at 200 °C. (i) Comparison of discharged energy density ($\eta > 90\%$) of this work and other reports at 200 °C.

results (Fig. S6). These results confirmed that the porous structure of ZIF-8 disrupted in the solvent and imidization (300 °C) process, thereby preventing defects between CT an PEI. The schematic diagram illustrating the resulting coordination interactions (Fig. 2e). As depicted in Fig. 2f and Fig. S9 (Supporting information), x mCT and PEI demonstrate similar glass transition temperature (T_g, 223.2–224.6 °C) and average inter-chain distance (5.36 Å).

Fig. S10 (Supporting information) shows the optical image and infrared spectrum of PEAA/0.5 mCT (where PEAA refers to polyether amide acid), providing evidence of coordination interactions occurring during the polycondensation process. As shown in Fig. 3a, the C=O peaks of PEAA and PEAA/0.5 mCT appears at 1719 cm^{-1} and 1713–1723 cm^{-1}, which can be ascribed to C=O coordination between C=O and Zn^{2+}. Additionally, PEAA/0.5 mCT exhibits a shoulder peak at 1196 cm^{-1} attributed to the lone pair electrons of C–O-C. Subsequently, the consistent C–N characteristic peaks were identified in Fig. S11 (Supporting information), confirming the complete imidization of x mCT. The SAXS scattering patterns and Porod curves of x mCT are depicted in Fig. S11 (Supporting information) and Fig. 3b. All samples exhibit positive deviation at the Porod curve tails, indicating the absence of sharp interface within x mCT. The ln(q)-ln($I(q)$) plot (Fig. 3c) shows that the D_m increases with mCT content, reaching a maximun of 3.04 for 0.5 mCT. This increased structural compactness is consistent with the wider bandgaps observed in UV–vis analysis (Fig. S13 in Supporting information), where PEI has a bandgap of 3.36 eV and 0.5 mCT reaches 3.48 eV. The coordination interaction between Zn and PEI in 0.5 mCT was analyzed using XAFS. Compared to the mCT, 0.5 mCT shows a lower WL energy position (labeled A and B in Fig. 3d) and a higher WL intensity (1.49 *vs.* 1.35), indicating a change in the electronic transition mode of the Zn element in mCT and 0.5 mCT. EXAFS analysis (Fig. 3e) reveals a reduced main peak intensity and slight peak broadening in 0.5 mCT, attributable to C=O-Zn coordination. The WT plot for 0.5 mCT (Fig. 3f) displays two lobes: a main lobe and a minor lobe are visible (Fig. 3f). The first one, localized in the $\triangle R = (1.0–2.2)$ Å and $\triangle k = (0–12)$ $Å^{-1}$ range. The second minor lobe collects the contributions coming from the Zn in ZIF-8 and the dimethylimidazole (2-MiM). Detailed coordination parameters for 0.5 mCT are provided in Table S1.

Fig. 4a shows the dielectric constant (ε_r) and loss (tanδ) of x mCT films measured at room temperature. The ε_r continuously increases with the content of mCT rising, for example, from 3.10 for the PEI to 3.73 for 1.0 mCT. Meanwhile, the tanδ of all polymer dielectrics remain below 0.015 across a frequency ranging of 10^2–10^6 Hz. Fig. S14 shows that the ε_r of all polymer dielectrics changes little from room temperature to 200 °C. As shown in Fig. S15 (Supporting information) and Fig. 4b, the introduction of the mCT leads to a significant reduction in the current density at high electric field and wide temperature range (25–200 °C), *e.g.*, from 7.2×10^{-7} A/cm^2 for PEI to 1.0×10^{-7} A/cm^2 for 0.5 mCT at 100 MV/m and 200 °C. The decrease of current density reduces the conduction loss when polymer dielectrics work at different temperatures, giving increase to an enhancement in the electrical breakdown strength (E_b) at different temperature. As shown in Fig. S16 (Supporting information) and Fig. 4c, the E_b of all films showed a decreasing trend with increasing temperature.

At 200 °C, the incorporation of the optimal loading ratio of mCT (0.5 wt%) increased the E_b to 594 MV/m compared to 399 MV/m for the PEI. More notably, 0.5 mCT exhibited a higher β value (18.26 for 0.5 mCT *vs.* 9.86 for PEI), indicating enhanced electric field resistance and dielectric reliability of the polymer dielectric under harsh conditions due to the introduction of mCT. The energy storage performance of polymer dielectrics at various temperatures (25, 150 and 200 °C) was obtained by electric displacement-electric field (*D-E*) loops (Figs. S17-S19 in Supporting information and Fig. 4d). The U_e of x mCT at different temperatures (25, 150 and 200 °C) are presented in Fig. S20 (Supporting information) and Fig. 4e, in which the high temperature energy storage performance of x mCT are improved compared to PEI. At 200 °C, the U_e with $\eta > 90\%$ reached 4.47 J/cm^3 for 0.5 mCT which is an improvement

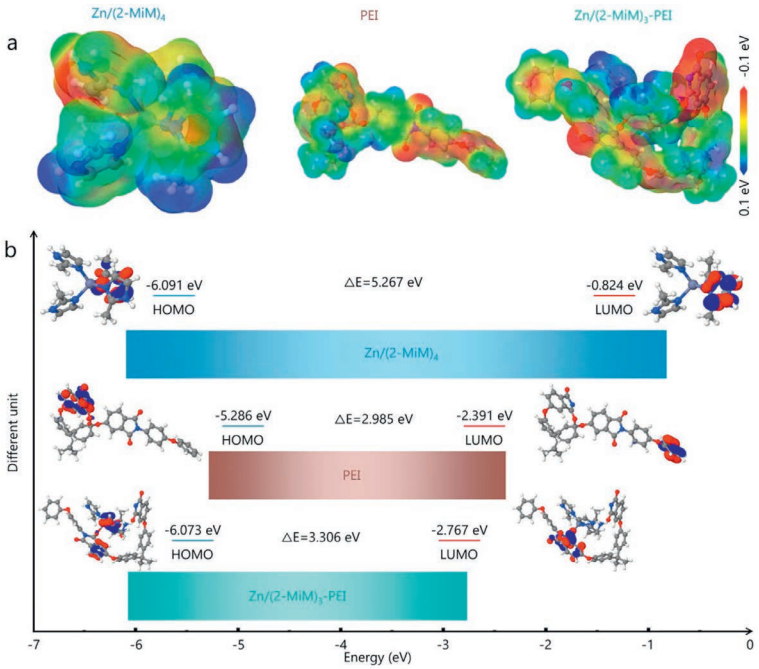


Fig. 5. (a) Electrostatic potential distribution of Zn-(2-MiM)$_4$ (ZIF-8 unit), PEI and Zn/(2-MiM)$_3$-PEI (C=O coordination between mCT and PEI). (b) Lowest unoccupied molecular orbital (LUMO) and highest occupied molecular orbital (HOMO) of Different unit.

of 728 % over that of PEI (0.54 J/cm^3). We prepared a large 0.5 mCT film of 12 × 18 cm^2 area (insert of Fig. 4f), and measured the breakdown and U_e at 600 MV/m and 200 °C at different regions. The results show high consistency across the different regions (573–640 MV/m and 4.32–4.71 J/cm^3). Cyclic charging-discharging tests at 150 and 200 °C were performed to examine the stability of 0.5 mCT. As shown in Fig. 4g, 0.5 mCT exhibits stable energy storage performance over 10^4 cycles under up to 150 and 200 °C at 300 MV/m. Furthermore, the U_e and η of 0.5 mCT polymer dielectric film were measured with different electrode diameters at 200 °C (Fig. 4h). It is found that the size of the electrodes has a negligible effect on the capacitive performance. Fig. 4i summarizes the U_e with $\eta \geq 90$ % at 200 °C and the electric field of 0.5 mCT and other advanced works. It is impressive that both the discharged energy density ~4.47 J/cm^3 and electric field ~594 MV/m for the 0.5 mCT outperform all the reported dielectric polymers and polymer nanocomposites [33,37–46].

In order to investigate the effect of interface bonding on molecular orbitals of polymer dielectrics. Density functional theory (DFT) was employed to analyze the interactions between ZIF-8 and PEI and HOMO-LUMO gap of 0.5 mCT. As shown in Fig. 5a, Zn in the Zn/(2-MiM)$_4$ (ZIF-8 unit) exhibits neutrality when coordinated tetrahedrally with 4 ligands. However, when ZIF-8 grows on the surface of CT, spatial hindrance effects can lead to lower coordination numbers and unoccupied orbitals of ZIF-8.

In the PEI molecular chain, the oxygen atoms of C=O groups (shown in red) possess lone pair electrons. The coordination bonds in Zn/(2-MiM)$_3$-PEI result from unoccupied orbitals of Zn and C=O lone pairs. The electrostatic potential of Zn/(2-MiM)$_3$-PEI is also depicted. Fig. 5b analyzes the HOMO and LUMO for Zn/(2-MiM)$_4$, PEI, and Zn/(2-MiM)$_3$-PEI, showing a HOMO-LUMO gap of 2.985 eV for PEI, which increases to 3.306 eV in Zn/(2-MiM)$_3$-PEI. This electrostatic distribution confirms the electron-donating role of C=O and the coordination structure between Zn and C=O, with the Zn/(2-MiM)$_3$-PEI composite showing a larger HOMO-LUMO gap, indicating that 0.5 mCT exhibits an improved insulating properties.

In summary, we propose a strategy of incorporating defects to significantly enhance the high-temperature capacitance of polymer-based dielectrics. The optimal polymer dielectric achieved an ultra-high U_e of 4.47 J/cm^3 with $\eta > 90$ % at 200 °C. Notably, the introduction of surface defects in nanosheets resulted in a more robust integration between the transitional MOF layer and nanosheets, as validated by XAFS. The DFT calculation indicate that MOF provides unoccupied orbitals to facilitate the formation of coordination bonds with C=O groups in the PEI chains, thereby increasing the HOMO-LUMO gap of 0.5 mCT. This study presents an innovative and effective method for enhancing the capacitance of polymer-based dielectrics in harsh conditions.

CRediT authorship contribution statement

Dongyang Chen: Writing – review & editing, Writing – original draft, Visualization, Validation, Software, Resources, Methodology, Investigation, Data curation, Conceptualization. **Xiaoxu Liu:** Writing – review & editing, Supervision, Project administration, Investigation, Funding acquisition, Conceptualization. **Haonan Chen:** Methodology, Investigation. **Yaru Wang:** Methodology. **Jing Li:** Visualization, Investigation. **Jiaming Sun:** Methodology, Investigation. **Xiaofeng Wang:** Writing – review & editing, Methodology, Investigation. **Qiong Liu:** Writing – review & editing.

Declaration of competing interest

The authors declare that they have no known competing financial interests or personal relationships that could have appeared to influence the work reported in this paper.

Acknowledgments

This work was supported by Key Laboratory of Engineering Dielectrics and Its Application (Harbin University of Science and Technology), Ministry of Education (No. KFM202503), Beijing Synchrotron Radiation 1W2A Work Station and 4B9A Work Station in China, Shanghai Synchrotron Radiation Facility BL01B Work Station, Natural Science Basic Research Program of Shaanxi (No. 2022JQ-405).

Supplementary materials

Supplementary material associated with this article can be found, in the online version, at doi:10.1016/j.cclet.2025.111436.

References

[1] H. Li, Y. Zhou, Y. Liu, et al., Chem. Soc. Rev. 50 (2021) 6369–6400.
[2] G. Wang, Z. Lu, Y. Li, et al., Chem. Rev. 121 (2021) 6124–6172.
[3] Z. Shang, X. An, S. Nie, et al., J. Bioresour. Bioprod. 8 (2023) 292–305.
[4] Y. Liu, K. Xiang, W. Zhou, et al., Small 20 (2024) 2308741.
[5] S. Zeng, G. Duan, R. Yu, et al., Prog. Mater. Sci. 147 (2025) 101356.
[6] X.Y. Wen, W. Li, H. Chen, et al., Rare Met. 44 (2025) 3881–3892.
[7] H. Zhang, X. Liu, et al., Chin. Chem. Lett. 37 (2026) 110790.
[8] T. Guo, L.B. Tang, W.N. Deng, et al., Rare Met. 44 (2025) 4631–4641.
[9] S. Jiang, J. Fang, H. Liu, et al., Chem. Eng. J. 502 (2024) 157745.
[10] H. Jin, T. Zhang, Z. Tian, et al., J. For. Eng. 9 (2024) 103–109.
[11] X.J. Liu, M.S. Zheng, G. Chen, et al., Energy Environ. Sci. 15 (2022) 56–81.
[12] H. Li, Y. Zhou, Y. Liu, et al., Chem. Soc. Rev. 50 (2021) 6369–6400.
[13] X. Wu, Y. Liu, X. Lin, et al., Surf. Interfaces 28 (2022) 101686.
[14] T. Zhang, Q. Chi, High temperature dielectric materials for electrical energy storage, in: B. Du (Ed.), Polymer Insulation Applied For HVDC Transmission, Springer, 2020, pp. 653–674.
[15] V. Adamec, J.H. Calderwood, J. Phys. D. Appl. Phys. 8 (1975) 551–560.
[16] J. Ho, T.R. Jow, IEEE Trans. Dielectr. Electr. Insul. 19 (2012) 990–995.
[17] Y. Zhu, P. Jiang, Z. Zhang, et al., Chin. Chem. Lett. 28 (2017) 2027–2035.
[18] R. Chen, X. Liu, N. Zhang, et al., Chin. Chem. Lett. 35 (2024) 109194.
[19] Q. Li, L. Chen, M.R. Gadinski, et al., Nature 523 (2015) 576–579.
[20] M. Yang, L. Zhou, X. Li, et al., Adv. Mater. 35 (2023) 2302392.
[21] X. Zhou, Q. Chen, Q.M. Zhang, et al., IEEE Trans. Dielectr. Electr. Insul. 18 (2011) 463–470.
[22] A. Azizi, M.R. Gadinski, Q. Li, et al., Adv. Mater. 29 (2017) 1701864.
[23] J. Dong, R. Hu, X. Xu, et al., Adv. Funct. Mater. 31 (2021) 2102644.
[24] Y. Zhou, Q. Li, B. Dang, et al., Adv. Mater. 30 (2018) 1805672.
[25] D. Ai, H. Li, Y. Zhou, et al., Adv. Energy Mater. 10 (2020) 1903881.
[26] B. Sun, P. Hu, X. Ji, et al., Small 18 (2022) 2202421.
[27] L.Z. Chen, D.D. Huang, Chin. Chem. Lett. 25 (2014) 279–282.
[28] C. Yuan, Y. Zhou, Y. Zhu, et al., Nat. Commun. 11 (2020) 3919.
[29] Y. Zhou, Y. Zhu, W. Xu, et al., Adv. Energy Mater. 13 (2023) 2203961.
[30] B. Zhang, X. ming Chen, Z. Pan, et al., Adv. Funct. Mater. 33 (2022) 2210050.
[31] S. Wang, Z. Luo, J. Liang, et al., ACS Nano 16 (2022) 13612–13656.
[32] J. Li, X. Liu, Y. Feng, et al., Energy Storage Mater. 54 (2023) 605–614.
[33] X. Liu, D. Chen, J. Li, et al., Adv. Mater. 36 (2024) 2402239.
[34] X. Xia, J. Yin, B. Su, et al., Compos. Part B: Eng. 120 (2017) 92–96.
[35] S.E. Neumann, J. Kwon, C. Gropp, et al., Science 383 (2024) 1337–1343.
[36] H. Li, B.S. Chang, H. Kim, et al., Joule 7 (2023) 95–111.
[37] Q. Zhang, X. Chen, B. Zhang, et al., Matter 4 (2021) 2448–2459.
[38] H. Li, D. Ai, L. Ren, et al., Adv. Mater. 31 (2019) 1900875.
[39] Y. Niu, J. Dong, Y. He, et al., Nano Energy 97 (2022) 107215.
[40] J. Song, H. Qin, S. Qin, et al., Mater. Horizon. 10 (2023) 2139–2148.
[41] A.A. Deshmukh, C. Wu, O. Yassin, et al., Energy Environ. Sci. 15 (2022) 1307–1314.
[42] W. Ren, M. Yang, L. Zhou, et al., Adv. Mater. 34 (2022) 2207421.
[43] C. Yuan, Y. Zhou, Y. Zhu, et al., Nat. Commun. 11 (2020) 3919.
[44] J. Dong, L. Li, P. Qiu, et al., Adv. Mater. 35 (2023) 2211487.
[45] M. Yang, L. Zhou, X. Li, et al., Adv. Mater. 35 (2023) 2302392.
[46] M. Yang, Y. Zhao, Z. Wang, et al., Energy Environ. Sci. 17 (2024) 1592–1602.